Monthly Notices of the ROYAL ASTRONOMICAL SOCIETY

MNRAS **509,** 738–747 (2022) https://doi.org/10.1093/mnras/stab2960
Advance Access publication 2021 October 14

Discovery of two bright high-redshift gravitationally lensed quasars revealed by *Gaia*

Christopher Desira [1,2]★ Yiping Shu [1,3,4] Matthew W. Auger,[1,2] Richard G. McMahon,[1,2] Cameron A. Lemon [5] Timo Anguita [6,7] and Favio Neira[6,7]

[1]*Institute of Astronomy, University of Cambridge, Madingley Road, Cambridge CB3 0HA, UK*
[2]*Kavli Institute for Cosmology, University of Cambridge, Madingley Road, Cambridge CB3 0HA, UK*
[3]*Max-Planck-Institut für Astrophysik, Karl-Schwarzschild-Straße 1, D-85740 Garching bei München, Germany*
[4]*Faculty of Physics and Astronomy, Astronomical Institute (AIRUB), German Centre for Cosmological Lensing, Ruhr University Bochum, D-44780 Bochum, Germany*
[5]*Institute of Physics, Laboratoire d'Astrophysique, Ecole Polytechnique Fédérale de Lausanne (EPFL), CH-1290 Versoix, Switzerland*
[6]*Departamento de Ciencias Fisicas, Universidad Andres Bello, Fernandez Concha 700, 7591538 Las Condes, Santiago, Chile*
[7]*Millennium Institute of Astrophysics, Monseñor Nuncio Sotero Sanz 100, Oficina 104, 7500011 Providencia, Santiago, Chile*

Accepted 2021 October 4. Received 2021 October 4; in original form 2021 July 28

ABSTRACT

We present the discovery and preliminary characterisation of two high-redshift gravitationally lensed quasar systems in *Gaia* Data Release 2 (DR2). Candidates with multiple close-separation *Gaia* detections and quasar-like colours in *WISE*, Pan-STARRS, and DES are selected for follow-up spectroscopy with the New Technology Telescope. We confirm DES J215028.71−465251.3 as a $z = 4.130 \pm 0.006$ asymmetric, doubly imaged lensed quasar system and model the lensing mass distribution as a singular isothermal sphere. The system has an Einstein radius of 1.202 ± 0.005 arcsec and a predicted time delay of ∼122.0 d between the quasar images, assuming a lensing galaxy redshift of $z = 0.5$, making this a priority system for future optical monitoring. We confirm PS J042913.17+142840.9 as a $z = 3.866 \pm 0.003$ four-image quasar system in a cusp configuration, lensed by two foreground galaxies. The system is well modelled using a singular isothermal ellipsoid for the primary lens and a singular isothermal sphere for the secondary lens with Einstein radii 0.704 ± 0.006 and 0.241 ± 0.030 arcsec, respectively. A maximum predicted time delay of 9.6 d is calculated, assuming lensing galaxy redshifts of $z = 1.0$. Furthermore, PS J042913.17+142840.9 exhibits a large flux ratio anomaly, up to a factor of 2.66 ± 0.37 in *i* band, that varies across optical and near-infrared wavelengths. We discuss LSST and its implications for future high-redshift lens searches and outline an extension to the search using supervised machine learning techniques.

Key words: gravitational lensing: strong – methods: observational – quasars: general.

1 INTRODUCTION

Strong gravitational lensing of high-redshift ($z \gtrsim 4$) quasars provides a number of unique ways to study the early universe. Time delay measurements between the lensed quasar components in this redshift regime allow us to determine the Hubble constant (H_0) in the epoch of deceleration, independent of distance ladder and CMB-based techniques (Refsdal 1966; Bonvin et al. 2016). Shear and magnification arising from lensing allows us to study the host galaxy properties that would normally be obscured by light from the quasar (Peng et al. 2006; Bayliss et al. 2017; Ding et al. 2017). Furthermore, microlensing by stars in the foreground galaxy on the source quasar and their lensed quasar images reveal the structure and temperature profile of the quasar accretion disc (Rauch & Blandford 1991; Jiménez-Vicente et al. 2015). Studying quasars and their host galaxies at high redshift, i.e. before the epoch of peak quasar activity ($z > 2.5$), is vital to understanding galaxy evolution and its relation to supermassive black hole (SMBH) growth (Salviander et al. 2006; Woo et al. 2006; Jahnke et al. 2009; DeGraf et al. 2015).

To date, 219 lensed quasar systems have been discovered and published in the scientific literature, with 83 (∼40 per cent) of those systems confirmed between 2018 and 2019 (Fig. 1, left-hand panel). The surge in discoveries was largely enabled by the second *Gaia* data release (Gaia Collaboration et al. 2018), which resolved and catalogued closely separated images, down to 0.4 arcsec (Arenou et al. 2018). There are still, however, fewer lensed quasars with source redshifts $z > 1.5$ than predicted by the quasar lens population model of Oguri & Marshall (2010), (Fig. 1, right-hand panel); this discrepancy is likely due to the anticorrelation between the lens galaxy brightness and source redshift (see Section 7). Furthermore, quasars at higher redshifts have similar mid-infrared (MIR) and optical colours to late-type stars, making the two populations difficult to separate. The lens population model predicts that there should be approximately seven strongly lensed quasars with apparent magni-

★ E-mail: cd612@cam.ac.uk

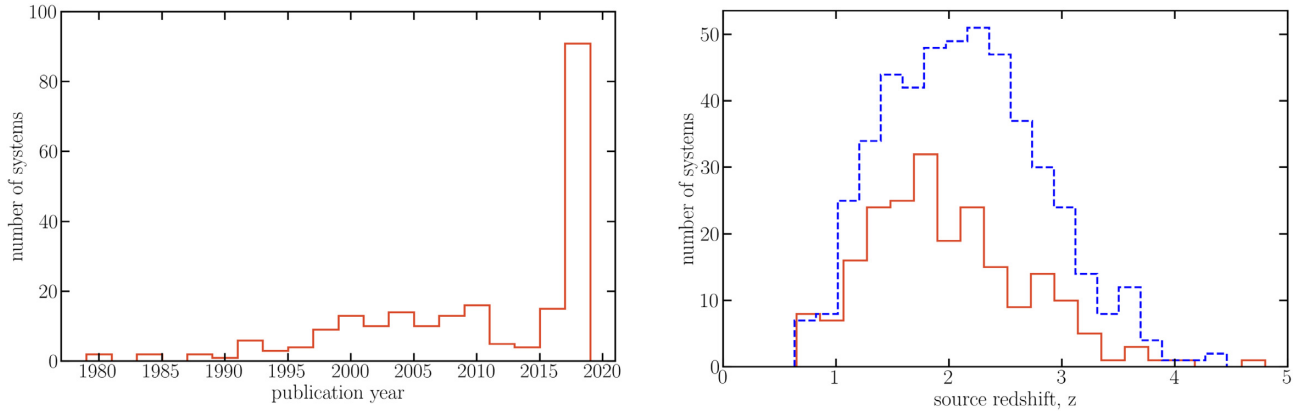

Figure 1. Left-hand panel: number of confirmed lensed quasar systems published per year with ∼40 per cent discovered between 2018 and 2019 using *Gaia* DR2. Right-hand panel: number of lensed quasars brighter than $G = 21.0$ and with separations >1 arcsec binned by source redshift for the known population (red) and predicted population (blue) as calculated by Oguri & Marshall (2010).

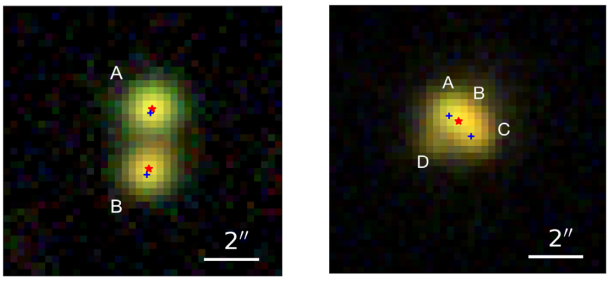

Figure 2. Left-hand panel: DES DR2 *gri* colour image of the confirmed double DES J2150−4652. Right-hand panel: PS1 *gri* colour image of the quad system PS J0429+1428. *Gaia* DR2 detections are overlaid as blue crosses and red stars indicate the position of the sources in their corresponding optical catalogues.

tudes brighter than the *Gaia* magnitude limit $G \sim 21$ mag and with a source redshift $z \geq 4$, however, to date only three such systems have been confirmed: SDSS J0946+1835, BRI 0952−0115, and PSS 2322+1944 (McMahon, Irwin & Hazard 1992; McGreer et al. 2010).

In this paper, we outline the first targeted search for high-redshift lensed quasars in *Gaia* DR2 (Gaia Collaboration et al. 2018) together with optical (DES and Pan-STARRS; Abbott et al. 2018; Chambers et al. 2019) and MIR (un*WISE*; Schlafly, Meisner & Green 2019) photometry. We present the discovery and confirmation of two new systems (Fig. 2) from the STRong lensing Insights into the Dark Energy Survey (STRIDES)[1] 2019–2020 follow-up campaign: DES J215028.71−465251.3, a lensed quasar with $z = 4.130 \pm 0.006$ at [right ascension (RA), declination (Dec.)] = (21:50:28.7, −46:52:51.3) and PS J042913.17+142840.9, a quad system with $z = 3.866 \pm 0.003$ at (RA, Dec.) = (04:29:13.2, +14:28:40.9). These systems will be referred to henceforth as DES J2150−4652 and PS J0429+1428.

[1]STRong lensing Insights into the Dark Energy Survey (STRIDES) collaboration, http://strides.astro.ucla.edu/.

2 LENS CANDIDATE SELECTION

2.1 *Gaia*

Gaia is an ESA space-based mission mapping the positions and motions of stars in the Milky Way with unrivalled astrometric precision (Gaia Collaboration et al. 2018). Although not its primary use-case, the telescope has proved useful for the detection of extragalactic point sources (Paine, Darling & Truebenbach 2018; Shu et al. 2019). We start our lens searches with the *Gaia* DR2 catalogue, which provides positions for ∼1.7 billion sources over the full sky down to a limiting magnitude of $G \sim 21.0$. *Gaia*'s high angular resolution (full width at half-maximum (FWHM) ∼ 0.1 arcsec) (Fabricius et al. 2016) allows us to resolve the individual quasar components of the lensed system, which would otherwise be blended in ground-based photometric catalogues.

For lensed quasar searches in *Gaia*, the catalogue can be made more manageable by removing areas of high stellar density. A local *Gaia* density cut ensures that, in addition to the Galactic Centre, other crowded regions are removed, i.e. star clusters, extended star-forming regions and the Magellanic Clouds. Since lensed quasars are at cosmological distances, their proper motions and parallaxes should be negligible; a simple cut on these parameters therefore provides an effective way of removing stellar contaminants and significantly reduces the catalogue size.

2.2 *Wide-Field Infrared Survey Explorer* (*WISE*)

WISE is a NASA MIR space telescope mapping the entire sky at wavelengths of 3.4, 4.6, 12, and 22 μm (*W*1, *W*2, *W*3, and *W*4) (Wright et al. 2010). In our selection, we apply $W1 - W2$ colour cuts that have repeatedly been shown to effectively separate quasars from stars, particularly at lower redshifts (Stern et al. 2012; Shu et al. 2019). Higher redshift quasars ($z > 3.5$), however, move to bluer colours in the MIR where the ∼1.0 μm minimum in the quasar spectral energy distribution (SED) shifts into the *W*2 band and the Hα emission line is redshifted to the *W*1 band (Richards et al. 2006; Stern et al. 2012). At these wavelengths, high redshift quasars become much more difficult to distinguish from early-type (M/L) stars (Fig. 3), and a simple $W1 - W2$ colour cut alone will result in a catalogue overwhelmed by false positives. Additionally, *WISE* has a much lower spatial resolution than other similar surveys.

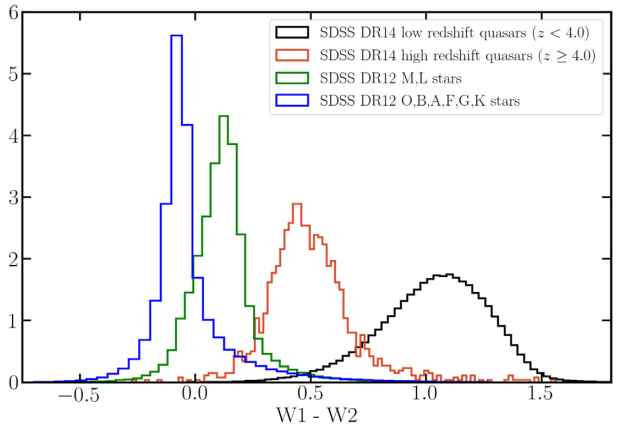

Figure 3. Distributions of un*WISE* $W1 - W2$ colours for SDSS DR14 (Pâris et al. 2018) high-redshift ($z \geq 4$) quasars, SDSS DR14 low-redshift ($z < 4$) quasars, SDSS DR12 (Alam et al. 2015) late-type (M/L) stars, and SDSS DR12 early-type stars (O, B, A, etc.). *W*1 and *W*2 are given in Vega magnitudes.

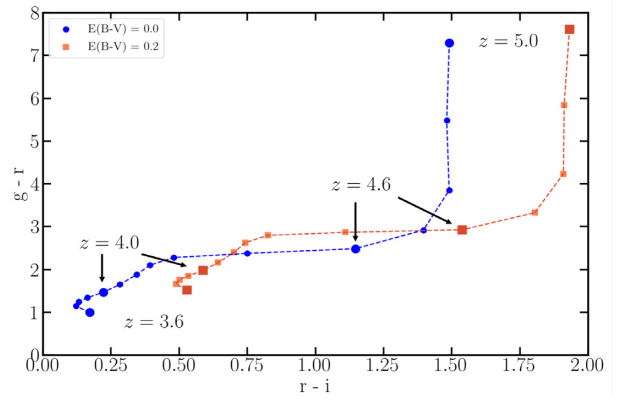

Figure 4. $g - r$ versus $r - i$ model colour tracks for quasars with redshifts $3.6 \leq z \leq 5.0$ calculated using quasar templates from Maddox et al. (2012). Tracks for $E(B - V) = 0$ in blue and $E(B - V) = 0.2$ in red.

The PSF FWHM of *W*1 and *W*2 is ∼6 arcsec, hence most lensed quasar systems are catalogued as a single source and light from the lensing galaxy may contaminate quasar $W1 - W2$ colours. In our searches, we used the un*WISE* photometric catalogue, which has a depth of 5σ and roughly 0.7 mag fainter than its precursor, All*WISE* (Schlafly et al. 2019).

2.3 Ground-Based Optical Photometry

In addition, single high-redshift quasars are also well separated from stars in optical colour space (Fan et al. 1999). At redshifts $3.6 < z < 4.6$, the *g*-band flux is suppressed by the Ly α forest and the *r* band is dominated by the intrinsic Ly α emission of the quasar. As redshifts increase, $g - r$ colours become redder until $z = 4.6$, when absorption begins to dominate in the *r* band. Reddening can also occur due to dust extinction intrinsic to the quasar, pushing $g - r$ and $r - i$ values even higher (see quasar model tracks, Fig. 4).

Although better than *WISE*, the typical resolution of ground-based imaging still does not always resolve the quasar images of lensed systems, and light from the lensing galaxy may contaminate $g - r$ and $r - i$ colours. Furthermore, the lensing galaxy is often hidden against the typically brighter quasars in the images themselves. By combining MIR colours with additional optical photometry, we can gain a more complete picture of the source SED and more effectively select lensed quasar candidates.

2.3.1 DES and Pan-STARRS

DES is a wide-field photometric survey spanning 5000 deg^2 of the Southern hemisphere and provides sub-arcsecond resolution and multiwavelength (*grizY*) imaging, sensitive over wavelengths 4000−11000 Å. We used the public DES Data Release 1 (DR1) photometric catalogue (Abbott et al. 2018) for candidate selection and the DES Data Release 2 (DR2) images[2] (Abbott et al. 2021) for photometric modelling.

Pan-STARRS (PS1) is an additional photometric survey providing *grizY* imaging complementary to DES. It covers approximately 30 000 deg^2 (e.g. nearly the entire sky north of Dec. −30°) and together with DES provides optical and near-infrared (NIR) photometry for ∼80 per cent of the total sky. Throughout this paper, we used the Pan-STARRS Data Release 1 (DR1) photometric catalogue and imaging (Chambers et al. 2019). In the following sections, we outline two independent lensed quasar searches, each leveraging one of these two imaging data sets.

2.4 Selection 1: *Gaia*-DES-un*WISE*

We started our lensed quasar search by cross matching the *Gaia* DR2 catalogue to DES DR1 using a 1 arcsec search radius and to un*WISE* using a 2 arcsec nearest-neighbour match. We selected sources with one or more additional catalogued *Gaia* components within an 8 arcsec radius and removed high-density regions by performing a local *Gaia* density cut <20 000 objects per deg^2, defined using a 128 arcsec radius. To remove stellar contaminants, we calculated proper motion significance and parallax significance as defined in Lemon, Auger & McMahon (2018). Sources with a proper motion significance >20 and a parallax significance >20 were removed before applying a latitude criterion of $|b| > 10°$ to remove sources near the Galactic plane. Sources with missing *griz* or *W*1, *W*2 flux measurements were removed from our candidate list. To determine an optimal threshold in $g - r$ versus $r - i$ and $z - W1$ versus $W1 - W2$ space, we compared known $z \geq 4$ quasars in SDSS DR14 to one million random *Gaia* sources with optical and MIR photometry. We corrected for Galactic extinctions using the reddening values in Schlafly & Finkbeiner (2011) and selected a boundary to achieve a quasar completeness of 91 per cent while removing 98 per cent of contaminants. We exclude objects where one of the following conditions are met:

$$g - r \leq 0.2, \tag{1}$$

$$g - r \leq 1.5 \ \& \ r - i \geq 0.5, \tag{2}$$

$$g - r \leq 2.1 \cdot (r - i) + 0.45 \ \& \ -0.1 \leq r - i \leq 0.5, \tag{3}$$

$$W1 - W2 \leq 0.12, \tag{4}$$

$$z - W1 \leq 2.7 \ \& \ W1 - W2 \geq 0.4, \tag{5}$$

$$z - W1 \leq -2.86 \cdot (W1 - W2) + 3.8 \ \& \ 0.12 \leq W1 - W2 \leq 0.4. \tag{6}$$

[2]See https://des.ncsa.illinois.edu/releases/dr2.

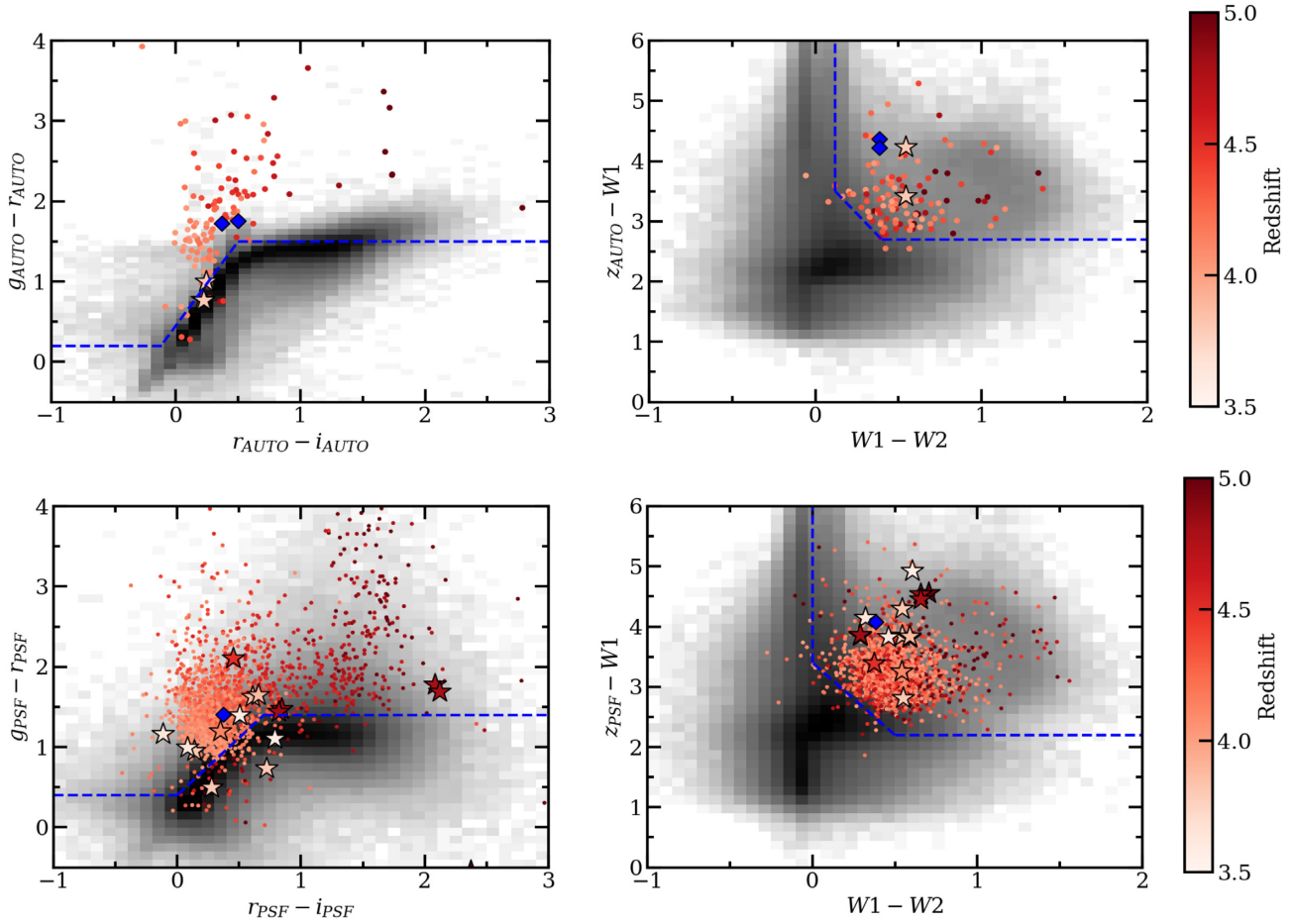

Figure 5. Colour selection criteria for the *Gaia*-DES-un*WISE* search (top panel) and *Gaia*-PS1-un*WISE* search (bottom panel). The two-dimensional (2D) histogram shows one million randomly selected *Gaia* sources in their corresponding optical surveys. The star and circle markers show where known high-redshift lensed quasar systems and SDSS quasars, respectively, lie in this colour space. Our selections are indicated with the blue dashed lines and our new discoveries with the blue diamond markers. DES/PS1 magnitudes are given in AB and corrected for Galactic extinction, whilst *WISE* magnitudes are given in Vega.

We grouped the remaining 6826 high-redshift candidates using a 6 arcsec radius and prioritised the resulting 113 groups with two or more components. This enriches the final candidate list for quadruply lensed systems and large separation doubles where the lensing galaxy is deblended.

2.5 Selection 2: *Gaia*-PS1-un*WISE*

We cross matched the *Gaia* DR2 catalogue to PS1 using a 1 arcsec search radius and performed a nearest-neighbour match to un*WISE* using a 2 arcsec radius. As in the DES search (Section 2.4), all sources with at least one additional *Gaia* detection within 8 arcsec were selected and stellar contaminants were removed using a proper motion significance >20 cut and a parallax significance >20 cut. High-density areas were also removed using a *Gaia* density cut of 20 000 per deg^2, defined using a 128 arcsec radius. We restricted the range to RA $\leq 240^\circ$ and Dec. $\leq 30^\circ$, reducing our catalogue size and ensuring that all sources were visible for spectroscopic follow-up in January 2020 (Section 4). An additional latitude criterion of $|b| > 10^\circ$ was applied to remove sources near the Galactic plane, and sources with missing flux measurements in PS1 and un*WISE* were removed. We corrected for Galactic extinction and defined our multidimensional optical and MIR colour cuts, as outlined in Section 2.4, by comparing known high-redshift SDSS quasars to random Gaia sources (Fig. 5). We exclude objects where one of the following conditions are met:

$$g - r \leq 0.4, \tag{7}$$

$$g - r \leq 1.4 \;\&\; r - i \geq 0.7, \tag{8}$$

$$g - r \leq 1.42 \cdot (r - i) + 0.4 \;\&\; 0.0 \leq r - i \leq 0.7, \tag{9}$$

$$W1 - W2 \leq 0.0, \tag{10}$$

$$z - W1 \leq 2.2 \;\&\; W1 - W2 \geq 0.5, \tag{11}$$

$$z - W1 \leq -2.4 \cdot (W1 - W2) + 3.4 \;\&\; 0.0 \leq W1 - W2 \leq 0.5. \tag{12}$$

We grouped the final 139 382 sources using a 6 arcsec radius and prioritised the 5116 groups with at least two components. Table 1 summarises candidate numbers after each stage of the DES and PS1 selections.

Table 1. Summary of lensed quasar selections for DES and Pan-STARRS searches. Candidate numbers are presented for each stage of the search.

Selection 1	Candidates
Gaia DR2-DES-un*WISE* xmatch + neighbour cuts	2250 852
Area and astrometry cuts	1160 476
Optical and MIR cuts	6826
Visual inspection, $n \geq 2$	113
Selection 2	
Gaia DR2-PS1-un*WISE* xmatch + neighbour cuts	20 346 008
Area and astrometry cuts	5527 081
Optical and MIR cuts	139 382
Visual inspection, $n \geq 2$	5116

3 VISUAL INSPECTION AND PIXEL MODELLING

As a final step, we visually inspected 113 *gri* colour cutouts from DES and 5116 from Pan-STARRS. Candidates were chosen primarily based on their image configurations and/or the presence of a putative lensing galaxy; however, the process is time consuming, prone to human error, and likely variable between individual inspectors. To remove the need for this step, a new automated approach is being developed using convolutional neural networks trained on simulated lensed quasar systems.

We selected the top candidates from the visual inspection stage and modelled their best-seeing single-epoch *griz* data to obtain approximate deblended photometry. Stacked data were not needed at this stage as all systems were optically bright. Model $g - r$ and $r - i$ colours were calculated and examined to ensure images were consistent with high-redshift quasars. The quasar images were fitted with PSFs, derived by fitting Moffat profiles to bright nearby stars. If visible, the lensing galaxy was fit using a Sérsic profile convolved with the PSF. The free parameters of the model are: the positions of the point sources as well as the lensing galaxy position, axis ratio, position angle, effective radius, and Sérsic index.

4 SPECTROSCOPIC CONFIRMATIONS

The candidates presented here (Fig. 2 and Table 2) were observed during two STRIDES lens follow-up campaigns in October 2019 and January 2020. Long-slit confirmation spectra were obtained for both targets using the ESO Faint Object Spectrograph and Camera 2 (EFOSC2; Buzzoni et al. 1984) on the 3.6 m New Technology Telescope (ESO programme ID: 0104.A-0194, PI: T. Anguita). We used a 1.2 arcsec slit with grism #13 providing spectral coverage over 3685–9315 Å, 2.77 Å/pixel dispersion and FWHM resolution of 21.2 Å. DES J2150−4652 was observed with a 900 s exposure at an average airmass of 1.1 and a slit position angle of $-3\overset{\circ}{.}6$ (East of North) allowing us to acquire spectra of both bright quasar images (Fig. 6). PS J0429+1428 was observed with a 900s exposure at an average airmass of 1.7 and a slit position angle of $+47\overset{\circ}{.}2$, which allowed the slit to pass through images A, B, and C. We applied a bias subtraction and flat fielding correction before wavelength calibrating using a HeAr lamp and response correcting using standard star observations. We removed cosmic rays using a peak finding algorithm, extracted the resulting 1D spectra (Fig. 7) and estimated the final redshifts. DES J2150−4652 clearly shows two traces exhibiting broad emission lines at the same redshift of $z = 4.130 \pm 0.006$. PS J0429+1428 is not well deblended but is clearly spatially resolved (i.e. extended) and the broad emission lines follow the full extent; likewise the absorption features are consistent across the full spatial extent of the trace. From the emission features, we infer a lensed quasar at redshift $z = 3.866 \pm 0.003$.

5 MODEL PHOTOMETRY AND MASS MODELLING

5.1 DES J2150−4652

To infer the magnitudes, positions, and corresponding uncertainties, we re-modelled our two confirmed systems using EMCEE (Foreman-Mackey et al. 2013) with the deepest and sharpest optical imaging available. We modelled DES J2150−4652 using stacked *griz* DES DR2 data, which has a photometric depth 0.45–0.7 mag deeper than

Table 2. Overview of catalogued astrometry and colours for newly discovered systems DES J2150−4652 and PS J0429+1428.

Name	RA (°)	Dec. (°)	*Gaia*, *G*	pmsig	plxsig	$g - r$	$r - i$	$z - W1$	$W1 - W2$
DES J2150−4652	327.619 619	−46.880 915	20.65, 21.14	1.812, nan	-0.362, nan	1.77, 1.74	0.51, 0.38	4.39, 4.24	0.38
PS J0429+1428	67.304 873	14.478 020	19.50, 20.05	nan, nan	nan, nan	1.79	0.62	4.65	0.38

Note. [a]The PSFMAG column was used for PS1 magnitudes and MAG_AUTO column for DES magnitudes. *WISE* positions are given as a proxy for the centres of the systems. 'nan' is a missing value marker returned by Gaia DR2.

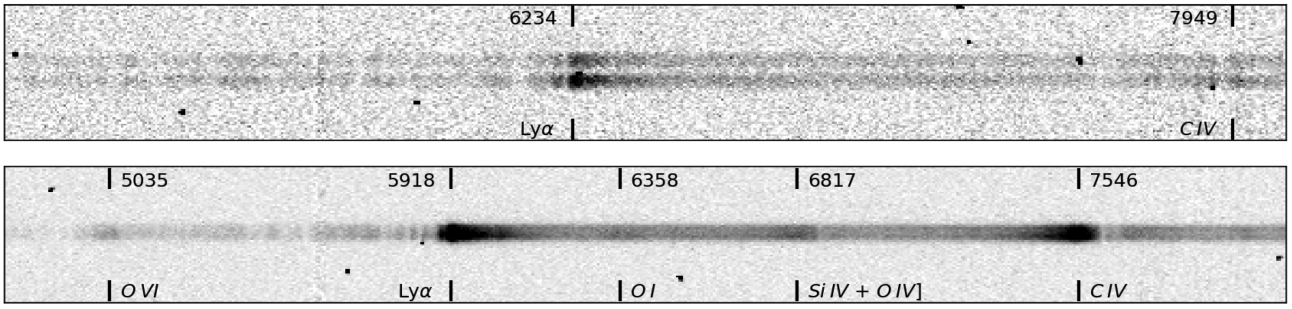

Figure 6. Spatially resolved NTT spectra for DES J2150−4652 (top panel) and PS J0429+1428 (bottom panel). The locations of prominent quasar emission lines and their observed wavelengths are indicated. Traces for DES J2150−4652 are well separated and show the same set of emission lines. PS J0429+1428 shows a single broad trace, which is due to three blended sources with the same emission lines.

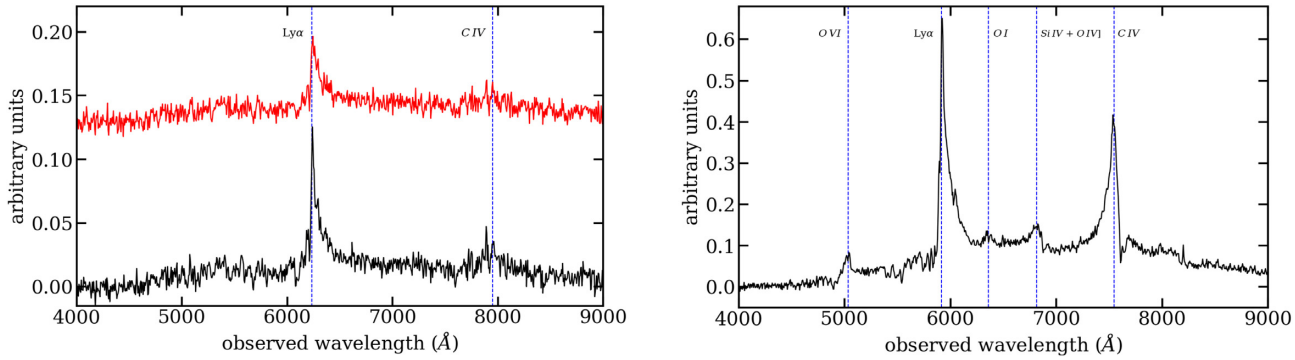

Figure 7. Extracted 1D NTT spectra for DES J2150−4652 (left-hand panel) and PS J0429+1428 (right-hand panel). Blue dashed lines indicate the locations of prominent quasar emission lines. DES J2150−4652 shows two separate traces with the fainter component (in red) shifted upwards. PS J0429+1428 shows a single trace of blended components (A+B+C) and multiple strong emission lines.

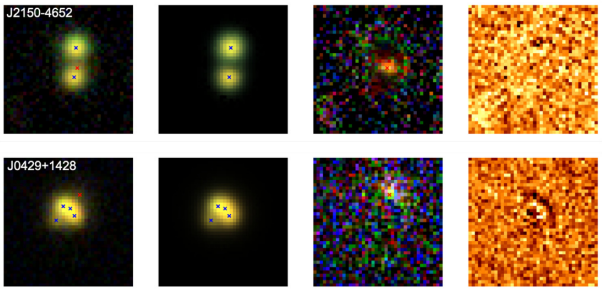

Figure 8. DES and PS1 pixel modelling for confirmed lenses. From the left-hand panel to right-hand panel: *gri* image, quasar model, image−quasar model, *i*-band residuals. The faint primary lens can be seen for DES J2150−4652 after subtracting the model quasar images and a faint secondary lens can be seen for PS J0429+1428.

DR1. In each band, the PSF was constructed by fitting nearby stars with two concentric Gaussians with the same angular parameters (i.e. position angle and axis ratio) but different FWHM. We fit the two quasars with a model consisting of two PSFs and, after inspecting the image residuals, we found an extended galaxy (Fig. 8). We interpret this galaxy as the lens and included it in the model as a Sérsic component convolved with the PSF. Table 3 lists the inferences for the model photometry.

We modelled the lensing mass distribution of DES J2150−4652 in the image plane as a singular isothermal sphere (SIS), fitting the model positions to the inferred photometric positions whilst accounting for the astrometric uncertainties on the observed positions. The full lens model therefore has five free parameters: lensing galaxy position (2), Einstein radius (1), and source position (2). We adopted a normal-distribution prior for the lens galaxy position based on its photometric position and uncertainty. As expected, this under-constrained model provides an excellent fit to the inferred quasar positions with $\chi^2 \sim 0.1$. Table 4 reports our inference on the mass model parameters.

5.2 PS J0429+1428

To infer *griz* photometry, we modelled the system using Pan-STARRS DR1 data. In addition, we modelled the positions separately using the wide, single-band *gri* filter data from the Canada–France–Hawaii Telescope (CFHT) (Fig. 9), which has a PSF FWHM of ∼0.65 arcsec and a pixel scale of 0.187 arcsec/pixel. As in Section 5.1, the PSF for the CFHT data is constructed by fitting nearby stars with two concentric Gaussians with the same angular parameters but different widths. The four quasar images were fitted with a model consisting of four PSFs, and although the residuals did not show any indication of the primary lensing galaxy, a faint galaxy to the north-west of the system can be seen (Fig. 8). We consequently re-modelled the CFHT data including this galaxy as a Gaussian surface brightness component to obtain astrometry for it. The robust positions of the quasars and galaxy inferred from the CFHT data were then used as priors for determining multiband photometry using the Pan-STARRS data. Due to the poor seeing of the Pan-STARRS data, all components were well modelled as point sources with Moffat surface brightness distributions, despite the galaxy being clearly extended in the CFHT data.

The lensing mass distribution was initially modelled in the image plane both as a singular isothermal ellipsoid (SIE) and as an SIS+shear model; however, neither of the mass models fit the data well, indicating a clear astrometric anomaly for one of the images. We concluded that the galaxy to the north-west was significantly contributing to the lensing, and we therefore include this galaxy in the mass model with a prior on the location given by the photometric position and uncertainty. The mass distribution was finally well modelled ($\chi^2 \sim 1.7$) with an SIE for the primary lens and a SIS for the secondary lens. There are 10 free parameters in this model: the galaxy positions (4, although the position of the secondary lens is constrained by the photometric position), Einstein radii (2), source position (2), and the axis ratio and position angle of the primary lens (2). Our best-fitting indicates an explicit degeneracy between the axis ratio of the primary lens, the Einstein radius of the secondary lens and the source position. Furthermore, we see no indication of the primary lensing galaxy in the photometric model residuals at the position inferred by our mass model or any other location. Fig. 10 shows the best-fitting lensing mass model for this system.

5.2.1 *Time delays and flux ratios*

We calculated flux ratios and predicted time delay between each of the images assuming a flat $\Omega_0 = 0.274$, $\Lambda_0 = 0.726$, $H_0 = 70.0\,\mathrm{km\,s^{-1}\,Mpc^{-1}}$ cosmology. We assume a fiducial lensing galaxy redshift of $z = 0.5$ for DES J2150−4652 and a higher redshift of $z = 1.0$ for both the primary and secondary galaxies in PS J0429+1428. A higher redshift for this system was chosen due to the lack of a visible primary lens indicating that the 4000 Å break has been

Table 3. Mean photometry and astrometry values with 1σ uncertainties for the newly discovered systems. DES J2150−4652 was modelled using DES DR2 and PS J0429+1428 was modelled using both PS1 DR1 and CFHT data. All magnitudes are given in the AB system.

Name	Component	g	r	i	z	δx (arcsec)	δy (arcsec)
DES J2150−4652	A	22.07 ± 0.04	20.37 ± 0.01	20.01 ± 0.01	20.13 ± 0.03	0.000 ± 0.006	0.000 ± 0.007
	B	22.53 ± 0.07	20.88 ± 0.03	20.54 ± 0.05	20.84 ± 0.14	−0.132 ± 0.006	−2.401 ± 0.006
	G	25.65 ± 0.87	22.95 ± 0.19	21.58 ± 0.14	20.80 ± 0.15	−0.029 ± 0.030	−1.920 ± 0.065
PS J0429+1428	A	21.07 ± 0.19	19.39 ± 0.05	18.97 ± 0.06	19.06 ± 0.10	0.000 ± 0.006	0.000 ± 0.004
	B	24.28 ± 2.23	19.73 ± 0.07	18.97 ± 0.05	19.08 ± 0.14	0.504 ± 0.007	−0.188 ± 0.006
	C	21.48 ± 0.21	19.65 ± 0.04	18.99 ± 0.04	18.91 ± 0.07	0.837 ± 0.004	−0.768 ± 0.004
	D	22.78 ± 0.44	20.88 ± 0.04	20.26 ± 0.03	20.16 ± 0.11	−0.570 ± 0.007	−1.083 ± 0.006
	G2	23.07 ± 0.40	22.49 ± 0.13	21.95 ± 0.12	21.62 ± 0.32	1.322 ± 0.030	1.027 ± 0.036

Table 4. Mean mass model parameter values with 1σ uncertainties for DES J2150−4652 and PS J0429+1428.

Name	α (arcsec)	δ (arcsec)	b (arcsec)	q	PA (°)
DES J2150−4652	−0.103 ± 0.006	−1.907 ± 0.063	1.202 ± 0.005	1.0	–
PS J0429+1428 (G1)	0.041 ± 0.009	−0.778 ± 0.007	0.704 ± 0.006	0.88 ± 0.01	+69.99 ± 3.31
PS J0429+1428 (G2)	1.320 ± 0.030	1.026 ± 0.035	0.241 ± 0.030	1.0	–

Note. [a]α = lens x position relative to image A, δ = lens y position relative to image A, b = Einstein radius, q = *axis ratio*, PA = position angle (east of north).

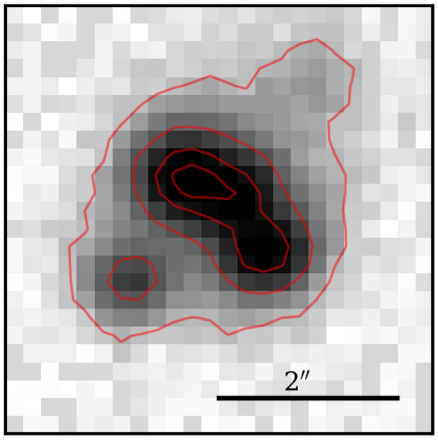

Figure 9. CFHT broadband *gri* (single-filter) image of PS J0429+1428 with contour plot overlaid in red. The faint secondary lensing galaxy can be seen to the north-west. The image was stacked using the MegaPipe stacking pipeline (Gwyn 2008).

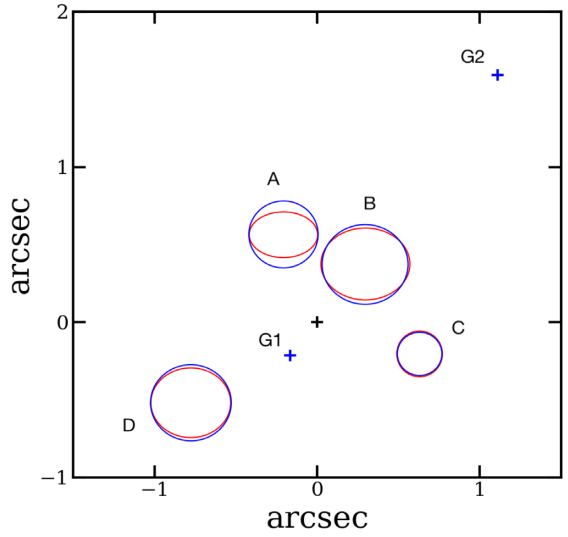

Figure 10. Gravitational lensing mass model for PS J0429+1428. Red circles are observed positions and uncertainties based on CFHT single-band *gri* data, blue circles are predicted positions and uncertainties, blue crosses are predicted galaxy positions, and the black cross is the predicted source position. For illustrative purposes, the image position uncertainties are increased by a factor of 75.

redshifted out of optical wavebands. We predict a 122.0 d time delay between the quasar images for DES J2150−4652 and a flux ratio (A/B) of 3.89 ± 0.67. Predicted time delays and flux ratios for PS J0429+1428 are outlined in Table 5.

5.2.2 *Undetected lens in PS J0429+1428*

We calculate the expected magnitudes of the undetected lensing galaxy, G1, using the inferred Einstein radius and spectroscopic redshift of the source. Assuming a flat ΛCDM cosmology and lens redshift, $z = 1.0$, we calculate an enclosed mass within the Einstein radius of, $M_{G1} = 1.9 \times 10^{11}$ $M_\odot$. We then use a 5 Gyr old stellar population model from Bruzual & Charlot (2003) to find mass-to-light ratios in the PS1 *griz* and CFHT broad *gri* filters. Finally, we assume that the lensing mass is comparable to the total stellar mass to determine the approximate expected magnitudes listed in Table 6.

6 DISCUSSION

6.1 DES J2150−4652

This doubly imaged quasar system has a source redshift $z = 4.130 \pm 0.006$ with a separation of 2.405 ± 0.009 arcsec and a faint but visible lensing galaxy 0.481 ± 0.065 arcsec North of quasar component B. The 1D and 2D NTT spectra show two well-separated traces with prominent Ly α and weak CIV emission lines (Figs 6 and 7). The system has two Gaia detections and one five-parameter solution where the proper motion significance and parallax significance are consistent with zero. The images are deblended in DES and have similar high-redshift quasar $g - r$ and $r - i$ model

Table 5. Predicted flux ratios with respect to image A and time delays for PS J0429+1428. Observed *i*-band flux ratios have been included for comparison.

Component	Flux ratio	Flux ratio (obs)	Time delay (d)			
			A	B	C	D
A	1.00 ± 0.00	1.00 ± 0.00	0.0	0.9	0.4	9.6
B	1.28 ± 0.05	1.00 ± 0.09	0.9	0.0	0.5	8.7
C	1.35 ± 0.07	0.98 ± 0.07	0.4	0.5	0.0	9.2
D	0.81 ± 0.10	0.30 ± 0.02	9.6	8.7	9.2	0.0

Table 6. Expected PS1 and CFHT magnitudes for the primary lensing galaxy, G1, in system PS J0429+1428, assuming a redshift of $z = 1.0$. The 5σ limiting magnitudes in each band are given for comparison.

Band	Predicted magnitude	5σ Magnitude limit
PS1 *g*	27.0	23.3
PS1 *r*	24.6	23.2
PS1 *i*	23.5	23.1
PS1 *z*	22.5	22.3
CFHT *gri*	24.7	24.6

colours (Table 3). The marginally constrained (due to the prior on the lens position) SIS model provides an almost perfect fit for the lensing mass distribution and we estimate the Einstein radius of the system to be 1.202 ± 0.005 arcsec. Image B is at a saddle point of the time delay surface, demagnified by 0.69 ± 0.16 relative to the source and Image A is at a minimum and magnified by 2.69 ± 0.16. The total overall magnification of the system is 3.38 ± 0.22. We calculated a long time delay of 122.0 d between the quasar images and a flux ratio (A/B) of 3.89 ± 0.67, a factor of 2.37 ± 0.42 times larger than the observed *i*-band flux ratio of 1.64 ± 0.07. This flux ratio anomaly is most likely due to the use of a simple SIS mass model. However, it may also be explained by the long time delay causing the quasars to be in significantly different variability phases, at the time of observation.

6.2 PS J0429+1428

This system was confirmed as a $z = 3.866 \pm 0.003$ quadruply lensed quasar in a cusp configuration with a maximum separation of 1.664 ± 0.009 arcsec. The 2D NTT (Fig. 6) spectrum shows a single broad trace and the reduced 1D spectrum (Fig. 7) shows several prominent emission lines, with CIV and SiIV+OIV] significantly affected by the presence of atmospheric A and B bands. The system has two Gaia detections and no proper motion or parallax measurements in DR2. We cross matched this object to Gaia Early Data Release 3 (Lindegren et al. 2020) and found one component with a proper motion significance of 5.0 and a parallax significance of 4.1. The quasar images are fully blended in PS1 and un*WISE* with colours consistent with a $z = 3.9 - 4.1$ quasar with reddening $E(B - V) \approx 0.2$. Modelling of higher resolution, deeper CFHT data (Fig. 9) shows no indication of the primary lensing galaxy but does reveal a secondary lens to the north-west. The system is well modelled using an SIE model for the primary lens with an Einstein radius of 0.704 ± 0.006 arcsec, axis ratio 0.88 ± 0.01 and position angle $+69\overset{\circ}{.}99 \pm 3.31$ and secondary lens with an SIS model with an Einstein radius 0.241 ± 0.030 arcsec. Images B and D are saddle points on the time delay surface and the system has a large total magnification of 57.59 ± 7.21. We find a discrepancy between the observed *i*-band flux ratio and the predicted flux ratio (A/D) of 2.66 ± 0.37, likely due to microlensing and/or differential reddening. Assuming a lens redshift $z = 1$, we calculate a maximum observed time delay between the quasar images A and D of only 9.6 days; similar relatively short predicted time delays are seen in other quad systems such as J0259−1635 (Schechter et al. 2018; Shajib et al. 2018). At this redshift, the primary lensing galaxy, G1, is expected to have a *z*-band magnitude slightly fainter than the PS1 stacked 5σ limit and a broadband *gri* magnitude slightly fainter than the 5σ limit of the CFHT imaging. Given the presence of the bright quasars and the uncertainty in our predicted magnitudes, these values are consistent with the non-detection of the galaxy in the imaging data and model residuals.

7 IMPLICATIONS AND FUTURE SEARCHES

Oguri & Marshall (2010) (OM10) provides a simulated catalogue of lensed quasars expected for the baseline survey planned with the Large Synoptic Survey Telescope (LSST; Ivezic et al. 2019). The catalogue is five times oversampled, complete with image configurations, lensing galaxy parameters and source parameters. By sampling 30 000 deg^2, we predict there should be approximately seven systems brighter than the Gaia limiting magnitude ($G = 21.0$) with $z \geq 4$ (five doubles and two quads) and 33 systems with $z \geq 3.5$ (25 doubles, 8 quads). This is in contrast to the current known lensed quasar population where only four systems with source redshift $z \geq 4$ and 10 systems with $z \geq 3.5$ above the Gaia limit have now been confirmed.[3]

The discrepancy between the numbers of predicted and confirmed systems may be due to the lack of a visible lensing galaxy in optical data. We predict that bright systems with low source redshifts $z < 3.5$ have a median lensing galaxy redshifts $z_{\rm lens} = 0.69$ and median *i*-band magnitude $i = 20.9$. By comparison, high source redshift systems $z \geq 3.5$ have a median lensing galaxy redshift $z_{\rm lens} = 1.14$ corresponding to a 3.5 times fainter median *i*-band magnitude $i = 22.4$ (Fig. 11). Moreover, lensing galaxies are extended, which make them even more difficult to detect next to the bright quasar images. Current photometric surveys such as Pan-STARRS provide stacked 5σ *i*-band depths of 23.1 mag, however future surveys such as LSST will go significantly deeper (after 1 yr, LSST should reach $i \sim 25.3$ mag) with better image quality, revealing the lensing galaxies for many more of these lensed quasar systems.

It is likely that high-redshift lensed quasars are better separated from other contaminant systems in higher dimensional spaces. Previous searches have explored using morphology independent supervised machine learning techniques such as Gaussian Mixture Models (GMMs) (Ostrovski et al. 2017) to separate systems with quasar, galaxy and star-like colours. We aim to improve upon our original selection by training a Random Forest (RF) classifier on

[3]This includes DES J2150−4652 and PS J0429+1428. A further 3 systems have also been confirmed with $z \geq 3.5$ but are too faint to be detected in *Gaia* DR2.

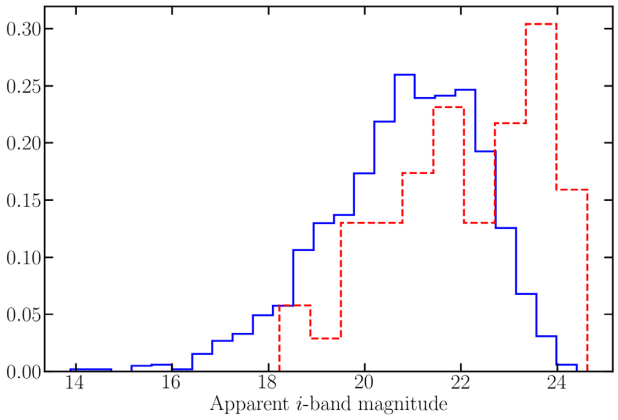

Figure 11. Normalised *i*-band magnitude distributions for OM10 lensing galaxies with source redshift $z \geq 3.5$ (red) and low source redshift systems $z < 3.5$ (blue). Only systems brighter than the *Gaia* limit are included.

a combination of morphological and photometric parameters to confirm and characterise the remaining high-redshift lensed quasar population in *Gaia*.

ACKNOWLEDGEMENTS

We would like to thank Paul Hewett, Matthew Temple, and Amy Rankine for helpful discussions regarding spectra and redshift estimation. CD and RM would like to acknowledge the science and technology facilities council (STFC) and the Kavli Foundation. YS acknowledges support from the Max Planck Society and the Alexander von Humboldt Foundation in the framework of the Max Planck-Humboldt Research Award endowed by the Federal Ministry of Education and Research. TA and FN acknowledge support from Proyecto Fondecyt N 1190335 and the ANID-Millennium Science Initiative Programme – ICN12_009 awarded to the Millennium Institute of Astrophysics MAS. This research is also supported by the European Research Council (ERC) under the European Union's Horizon 2020 research and innovation programme (grant agreement No 787886).

This work has made use of data from the European Space Agency (ESA) mission *Gaia* (https://www.cosmos.esa.int/gaia), processed by the *Gaia* Data Processing and Analysis Consortium (DPAC, https://www.cosmos.esa.int/web/gaia/dpac/consortium). Funding for the DPAC has been provided by national institutions, in particular the institutions participating in the *Gaia* Multilateral Agreement.

This publication makes use of data products from the Wide-field Infrared Survey Explorer, which is a joint project of the University of California, Los Angeles, and the Jet Propulsion Laboratory/California Institute of Technology, funded by the National Aeronautics and Space Administration.

The Pan-STARRS1 Surveys (PS1) and the PS1 public science archive have been made possible through contributions by the Institute for Astronomy, the University of Hawaii, the Pan-STARRS Project Office, the Max-Planck Society and its participating institutes, the Max Planck Institute for Astronomy, Heidelberg and the Max Planck Institute for Extraterrestrial Physics, Garching, The Johns Hopkins University, Durham University, the University of Edinburgh, the Queen's University Belfast, the Harvard–Smithsonian Center for Astrophysics, the Las Cumbres Observatory Global Telescope Network Incorporated, the National Central University of Taiwan, the Space Telescope Science Institute, the National Aeronautics and Space Administration under Grant No. NNX08AR22G issued through the Planetary Science Division of the NASA Science Mission Directorate, the National Science Foundation Grant No. AST-1238877, the University of Maryland, Eotvos Lorand University (ELTE), the Los Alamos National Laboratory, and the Gordon and Betty Moore Foundation.

This project used public archival data from the Dark Energy Survey (DES). Funding for the DES Projects has been provided by the U.S. Department of Energy, the U.S. National Science Foundation, the Ministry of Science and Education of Spain, the Science and Technology Facilities Council of the United Kingdom, the Higher Education Funding Council for England, the National Center for Supercomputing Applications at the University of Illinois at Urbana-Champaign, the Kavli Institute of Cosmological Physics at the University of Chicago, the Center for Cosmology and Astro-Particle Physics at the Ohio State University, the Mitchell Institute for Fundamental Physics and Astronomy at Texas A&M University, Financiadora de Estudos e Projetos, Fundação Carlos Chagas Filho de Amparo à Pesquisa do Estado do Rio de Janeiro, Conselho Nacional de Desenvolvimento Científico e Tecnológico and the Ministério da Ciência, Tecnologia e Inovação, the Deutsche Forschungsgemeinschaft, and the Collaborating Institutions in the Dark Energy Survey. The Collaborating Institutions are Argonne National Laboratory, the University of California at Santa Cruz, the University of Cambridge, Centro de Investigaciones Energéticas, Medioambientales y Tecnológicas-Madrid, the University of Chicago, University College London, the DES-Brazil Consortium, the University of Edinburgh, the Eidgenössische Technische Hochschule (ETH) Zürich, Fermi National Accelerator Laboratory, the University of Illinois at Urbana-Champaign, the Institut de Ciències de l'Espai (IEEC/CSIC), the Institut de Física d'Altes Energies, Lawrence Berkeley National Laboratory, the Ludwig-Maximilians Universität München, and the associated Excellence Cluster Universe, the University of Michigan, the National Optical Astronomy Observatory, the University of Nottingham, The Ohio State University, the OzDES Membership Consortium, the University of Pennsylvania, the University of Portsmouth, SLAC National Accelerator Laboratory, Stanford University, the University of Sussex, and Texas A&M University. Based in part on observations at Cerro Tololo Inter-American Observatory, the National Optical Astronomy Observatory, which is operated by the Association of Universities for Research in Astronomy (AURA) under a cooperative agreement with the National Science Foundation. Based on observations obtained with MegaPrime/MegaCam, a joint project of CFHT and CEA/DAPNIA, at the Canada–France–Hawaii Telescope (CFHT) which is operated by the National Research Coun cil (NRC) of Canada, the Institut National des Science de lÚnivers of the Centre National de la Recherche Scientiffique (CNRS) of France, and the University of Hawaii. The observations at the Canada–France–Hawaii Telescope were performed with care and respect from the summit of Maunakea, which is a significant cultural and historic site. This research made use of Astropy,[4] a community-developed core PYTHON package for Astronomy (Astropy Collaboration et al. 2013, 2018).

DATA AVAILABILITY STATEMENT

All data underlying this article are public. The following tables were used: des_dr1 (NCSA DESaccess archive), StackObjectThin (downloaded via Casjobs), *gaia*_source (Gaia archive), and un*WISE* band-merged (downloaded directly from the un*WISE* website). DES

[4]http://www.astropy.org

DR1/DR2 images can be downloaded from the NCSA DESaccess archive and PS1 images via the PS1 image cutout interface. NTT spectra and calibration data are available via the ESO Science Archive Facility (see programmeID: 0104.A-0194, nights: 2019 October 24 and 2020 January 20.)

REFERENCES

Abbott T. M. C. et al., 2021, Astrophys. J. Suppl. Ser., 255, 29
Abbott T. M. C. et al., 2018, ApJS, 239, 18
Alam S. et al., 2015, ApJS, 219, 12
Arenou F. et al., 2018, A&A, 616, A17
Astropy Collaboration et al., 2013, A&A, 558, A33
Astropy Collaboration et al., 2018, AJ, 156, 123
Bayliss M. B. et al., 2017, ApJ, 845, L14
Bonvin V. et al., 2016, MNRAS, 465, 4914
Bruzual G., Charlot S., 2003, MNRAS, 344, 1000
Buzzoni B. et al., 1984, The Messenger, 38, 9
Chambers K. C. et al., 2019, The Pan-STARRS1 Surveys, preprint (arXiv: 1612.05560)
DeGraf C., Di Matteo T., Treu T., Feng Y., Woo J. H., Park D., 2015, MNRAS, 454, 913
Ding X. et al., 2017, MNRAS, 472, 90
Fabricius et al., 2016, A&A, 595, A3
Fan X. et al., 1999, AJ, 118, 1
Foreman-Mackey D., Hogg D. W., Lang D., Goodman J., 2013, PASP, 125, 306
Gaia Collaboration et al., 2018, A&A, 616, A1
Gwyn S. D. J., 2008, PASP, 120, 212
Ivezic e. et al., 2019, ApJ, 873, 111
Jahnke K. et al., 2009, ApJ, 706, L215
Jiménez-Vicente J., Mediavilla E., Kochanek C. S., Muñoz J. A., 2015, ApJ, 799, 149
Lemon C. A., Auger M. W., McMahon R. G., 2018, MNRAS, 483, 4242
Lindegren L. et al., 2020, A&A, 649, 35
McGreer I. D. et al., 2010, AJ, 140, 370
McMahon R., Irwin M., Hazard C., 1992, GEMINI Newsl. R. Greenwich Obs., 36, 1
Maddox N., Hewett P. C., Péroux C., Nestor D. B., Wisotzki L., 2012, MNRAS, 424, 2876
Oguri M., Marshall P. J., 2010, MNRAS, 405, 2579
Ostrovski F. et al., 2017, MNRAS, 465, 4325
Paine J., Darling J., Truebenbach A., 2018, ApJS, 236, 37
Pâris I. et al., 2018, A&A, 613, A51
Peng C. Y. et al., 2006, ApJ, 649, 616
Rauch K. P., Blandford R. D., 1991, ApJ, 381, L39
Refsdal S., 1966, MNRAS, 132, 101
Richards G. T. et al., 2006, ApJS, 166, 470
Salviander S., Shields G. A., Gebhardt K., Bonning E. W., 2006, New Astron. Rev., 50, 803
Schechter P. L., Anguita T., Morgan N. D., Read M., Shanks T., 2018, Res. Notes Am. Astron. Soc., 2, 21
Schlafly E. F., Finkbeiner D. P., 2011, ApJ, 737, 103
Schlafly E. F., Meisner A. M., Green G. M., 2019, ApJS, 240, 30
Shajib A. J. et al., 2018, MNRAS, 483, 5649
Shu Y., Koposov S. E., Evans N. W., Belokurov V., McMahon R. G., Auger M. W., Lemon C. A., 2019, MNRAS, 489, 4741
Stern D. et al., 2012, ApJ, 753, 30
Woo J.-H., Treu T., Malkan M. A., Bland ford R. D., 2006, ApJ, 645, 900
Wright E. L. et al., 2010, AJ, 140, 1868

This paper has been typeset from a TEX/LATEX file prepared by the author.